Effects of Surface Scattering in Waveform Inversion

Florian Bleibinhaus, Stéphane Rondenay

Massachusetts Institute of Technology, Department of Earth, Atmospheric and Planetary Sciences, Earth Resources Laboratory, 77 Massachusetts Ave 54-612, Cambridge, MA 02139, USA, bleibi@mit.edu, rondenay@mit.edu

Abstract

In full waveform inversion of seismic body waves, the free surface is often ignored on grounds of computational efficiency. We investigate the effect of this simplification for highly irregular topography by means of a synthetic example. Our test model and data conform to a long-offset survey of the upper crust in terms of size and frequency. Random fractal variations are superimposed on a background model. We compute synthetic data for this model and different topographies, and we invert it neglecting the free surface. The resulting waveform models are relatively similar and, for the most part, show a high degree of correlation with the true model. The inversion of the irregular-topography data produces a few strong artifacts at shallow depths, but only a minor decrease in overall resolution. However, both waveform models fail to image below a strong shallow velocity contrast. The results suggest that in this part of the model the incapacity to properly reproduce the reverberations from that contrast without free surface derails both inversions.

Introduction

One of the major obstacles to applying waveform inversion is the computational expense of the forward solution. For most practical cases severe simplifications are employed in order to make the inversion feasible. Regional seismology studies often use the reflectivity method, which assumes laterally invariant, layered media (e.g. Xu and Wiens, 1997; Gu et al., 2005). Kaslilar (2007) and Campman and Riyanti (2007) use a superposition of small-scale heterogeneities on a laterally invariant embedding medium to invert scattered surface waves. In controlled source seismology the most popular forward solutions are finite difference frequency domain methods, mostly in a 2D viscoacoustic, isotropic implementation (e.g. Pratt, 1999; Hicks and Pratt, 2001; Operto et al., 2004; Ravaut et al., 2004; Operto et al., 2006; Bleibinhaus et al., 2007; Gao et al., 2007). The free surface is often ignored not only because modeling irregular topography is computationally extremely expensive, but also because modeling of free surface multiples requires extremely accurate background velocity and attenuation information, and also accurate correction factors for the geometric spreading of multiples, if the modeling is in 2D (Hicks and Pratt, 2001).

One consequence of such simplifications is that data preparation for waveform inversion is primarily about reducing and adapting the waveforms, such that the preprocessed wavefield complies with the forward scheme. However, the remaining fraction of the wavefield that cannot be modeled will inevitably blur the recovered structure. Due to the non-linearity of waveform inversion, the degradation is difficult

to predict. Understanding the impact of the various simplifications in order to assess the uncertainty of waveform models is all the more important.

This study investigates effects of neglecting the free surface in waveform inversion. Pratt (1999) obtained good results from the inversion of lab data acquired on the flat surface of a physical scale model in a water tank, although he used absorbing boundary conditions. Brenders and Pratt (2007) also used absorbing boundary conditions when they inverted synthetic crustal-scale refraction data generated with a free surface by a third party, and they were able to image the model, which was not disclosed to them, with great detail. Operto et al. (2004) and Bleibinhaus et al. (2007) report good results, although they neglected the free surface condition in the inversion of data acquired in mountainous regions with irregular topography. However, Bleibinhaus et al. also noted several artifacts in their waveform models, the source of which remained unclear. Aside from data quality issues like S/N or spatial aliasing, using an absorbing boundary instead of an irregular free surface condition could be responsible. Other possibilities include, but are not limited to, ignoring attenuation, 3D variations, anisotropy, and P-S conversions. The indications that ignoring free surface effects may play the crucial role in limiting the success of waveform inversion in this case are: the highly irregular topography of this survey, the prevalence of a strong P coda (Figure 1), possibly the result of surface scattering, and spurious phases in the synthetic data from waves that appear to be propagating above ground.

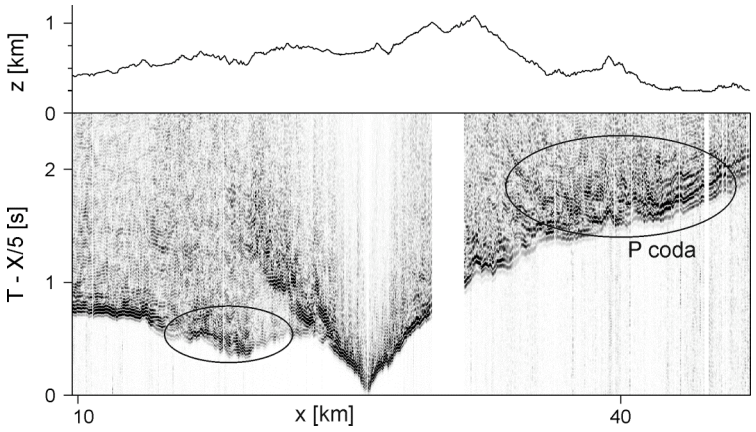

Figure 1: Bandpass-filtered time-reduced shot gather from the San-Andreas-Fault survey, elevation on top (V.E. 5). Note the strong coda. It may be caused by intrinsic scattering, but also by surface scattering, conversion and near-surface multiples.

The comparison of sensitivity kernels computed with absorbing boundaries and with a free, irregular surface (Figure 2) underscores this concern. Although much of the small scale variations of the irregular-topography kernel would be suppressed during the inversion by regularization filters, the differences appear significant enough to cause strong artifacts.

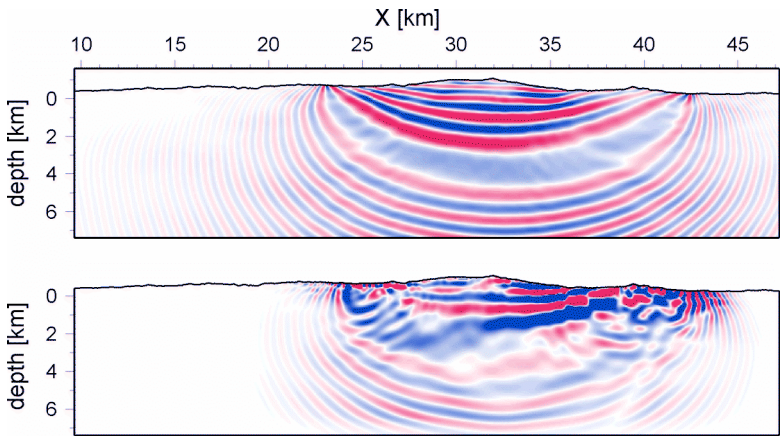

Figure 2: Monochromatic (4 Hz) kernel for one source-receiver pair computed in the smooth waveform inversion starting model of Bleibinhaus et al. (2007) with the frequency-domain code of Pratt (1999) using absorbing boundaries (top), and with the visco-elastic time-domain code of Robertsson (1996) and irregular topography (bottom). The time-domain kernel was computed for a time window of 1.5 s after the first arrival. The windowing explains the zero sensitivity of this kernel at greater depth/distance, and its complexity is the result of scattering and conversion at the irregular free surface.

Test model

We created a synthetic test model by superposing fractal wave speed variations of +/- 0.8 km/s onto a relatively smooth background model, which varies from 1.6 to 6.4 km/s (Figure 3). The background model reflects the complex structure across the San Andreas Fault in Central California. A geologically realistic vp/vs model was created by filtering the velocity model and adding long wavelength random variations. Quality factors for pressure waves were constructed in a similar way. Densities were derived from the velocity model using Gardner's (1974) formula, and adding 3% random variations. The resulting model exhibits a fair amount of heterogeneity on all scale lengths. It is representative for very complex geological situations. In particular, it features a shallow, strong, first-order discontinuity in one part of the model.
Two models were derived from the parameter distributions displayed in Figure 3 by (a) adding a flat free surface at 750 m elevation, and (b) by adding irregular topography ranging from 200m to 1100 m elevation, taken from the San-Andreas-Fault-survey receiver elevation values (Figure 1).

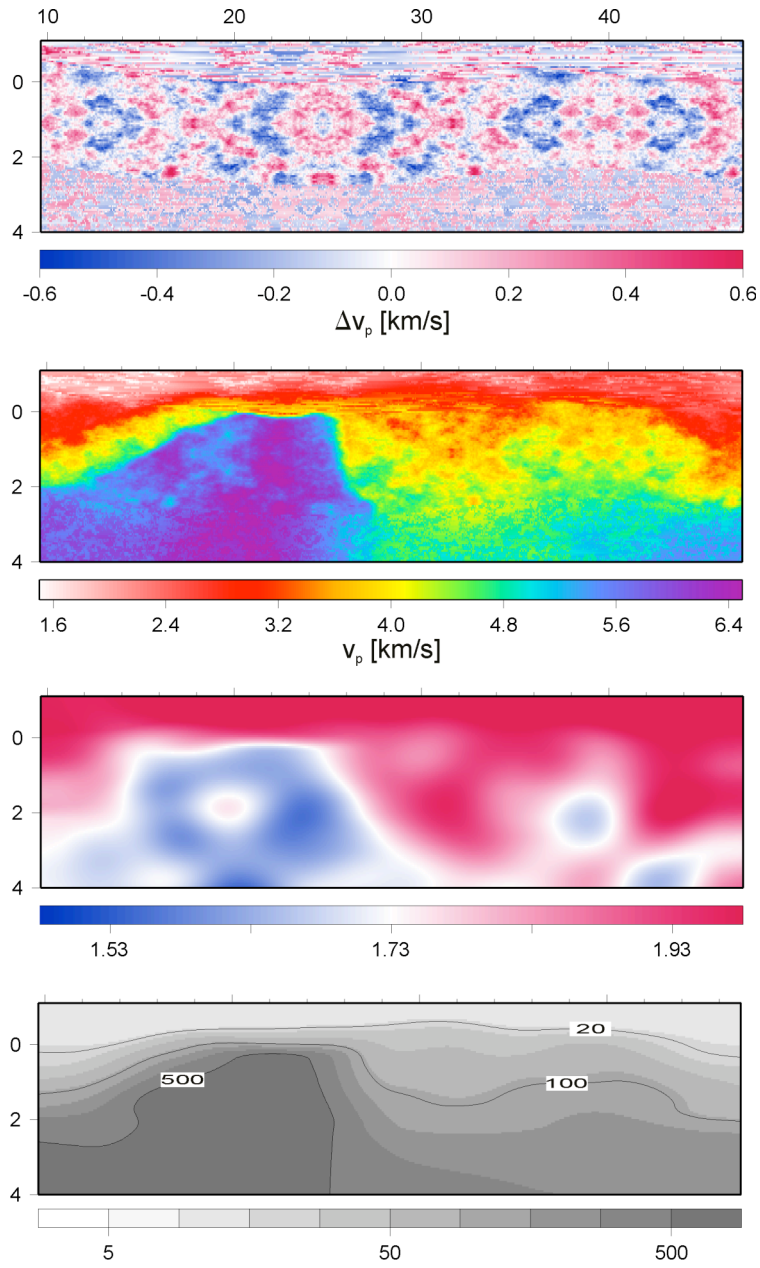

Figure 3: Synthetic model. Fractal p-wave speed perturbations, p-wave speed, Vp/Vs ratio, Qp (from top to bottom). The background velocity model is similar to the structure found across the San Andreas Fault in Central California with granite to the SW of the fault (high velocities at km 10-27) and sediments to the NE (low velocities at km 26-50). Shear wave speed is relatively low in the shallow sediments, and relatively high in the granite. (For convenience, we will use these geologic terms throughout the paper). The quality factor for p-waves ranges from 10 at the surface to 600, Qs is half that value. The model size is 37.5 km * 7.5 km with a grid spacing of 15 m. (The lower portion of the model is not shown.)

Forward modeling

The synthetic data was produced with the visco-elastic finite-difference time-domain code of Robertsson et al. (1994; 1996; 1997). The free surface is simulated with the image method. Benchmark tests (Robertsson, 1996) suggest that topography must be sampled with at least 15 grid points per minimum wavelength. We use a 5 Hz Ricker

wavelet as source, which generates frequencies of up to 15Hz, implying that ~ 7 m grid spacing is required. After some testing, we decided on 5 m grid spacing at and near the surface. Wavelets computed for 2.5 m grid spacing are well in phase with the 5 m solution, although they differ by 10% RMS amplitude. In contrast, the wavelets for the 10 m solution are out of phase resulting in 50% RMS amplitude error. In general the solution converges for decreasing grid spacing, and the choice of 5 m is based on the trade-off between accuracy and computation time. At greater depth the grid spacing is increased to 15 m to save computation time.

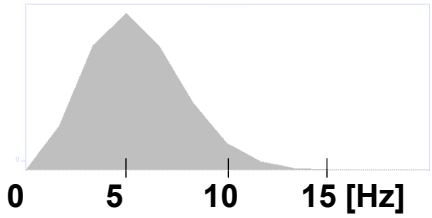

Figure 4: Amplitude spectrum of the 5 Hz Ricker source wavelet. Note that for computational reasons this wavelet is of considerably lower frequency than the real source (3-60 Hz). This is necessary in order to avoid excessive computation times by having to decrease the grid spacing, but also sufficient because we intend to use frequencies from 3 to 15 Hz in the inversion.

76 synthetic shot sections were computed at 500 m spacing for a 37.5 km long stationary receiver array at 50 m spacing for the flat-surface and the irregular-topography test models. The computation time for one survey amounts to one day on a 25-node cluster. Figure 5 shows an exemplary shot section. The irregular-topography data shows a significant amount of scattering and static shifts. Note that the irregular-topography data and the real data (Figure 1) cannot be compared directly due to the missing high frequencies in the synthetic source wavelet (Figure 4).

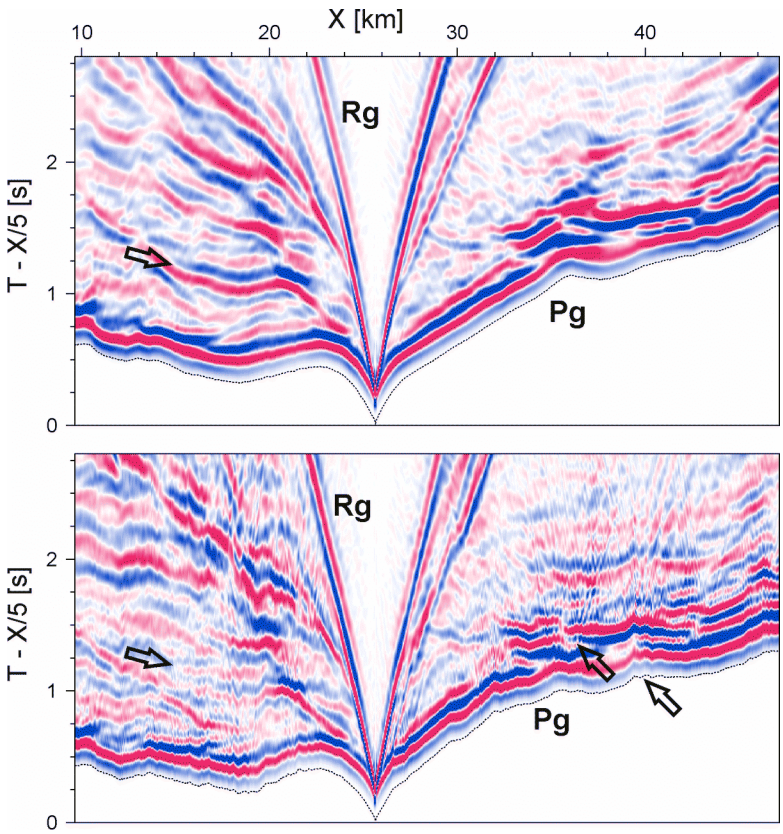

Figure 5: Trace-normalized reduced shot sections at km 26, vertical component, computed for a flat surface (top) and irregular topography (bottom). Dotted line is first arrival picks. Traveltimes between the two shots differ by up to 0.2 s. In addition, some secondary phases virtually disappeared in the irregular-topography data, or are significantly scattered.

Data preparation

The purpose of data preparation for waveform inversion is to exclude parts of the data that cannot be reproduced by the physics of the forward modeling, and to mitigate the impact of those parts of the data that are too complex to be predicted during the first iterations of the inversion. For this study, the data was windowed around the first break, and the near offsets were excluded (Figure 6). The remaining energy corresponds mostly to P-waves.

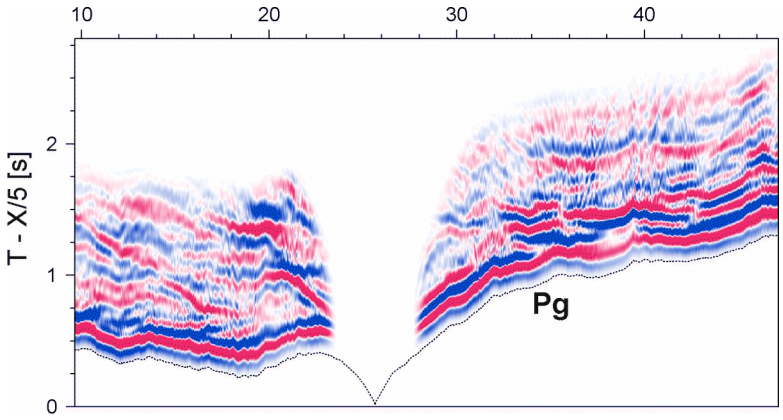

Figure 6: Preprocessed shot gather of Figure 5. Traces were muted 1.5 s after the first arrivals with a 200 ms taper, and the near offsets (2.5 km) were excluded from the inversion. Remaining shear waves in the offset range 2.5 – 5 km were removed by an offset dependent mute window. Dotted line is first arrival picks.

Starting model

Waveform inversion requires a relatively accurate starting model, depending on the wavelength of the data (Pratt et al., 1996). The source wavelet used in this study provides significant energy below 1 Hz (Figure 4). However, we want to mimic realistic conditions for controlled source refraction seismology, which means that we cannot use frequencies below 3 Hz (Bleibinhaus et al., 2007). Real applications and synthetic studies with realistic data frequencies have shown that starting models derived from traveltime tomography are both, required and sufficient, to meet the accuracy demands of waveform inversion (e.g. Pratt, 1999; Sirgue and Pratt, 2004). We performed a damped least-squares inversion, using the eikonal solver of Hole (1992) to compute travel-times and the flexible inversion grid parameterization of Bleibinhaus and Gebrande (2006). Since the data is noise-free, first-arrivals could be picked automatically. For simplicity, we used the flat-surface dataset. The results of the traveltime inversion are displayed in Figure 7 and Figure 8. As a final step, the velocity values in areas without ray coverage were replaced by extrapolation.

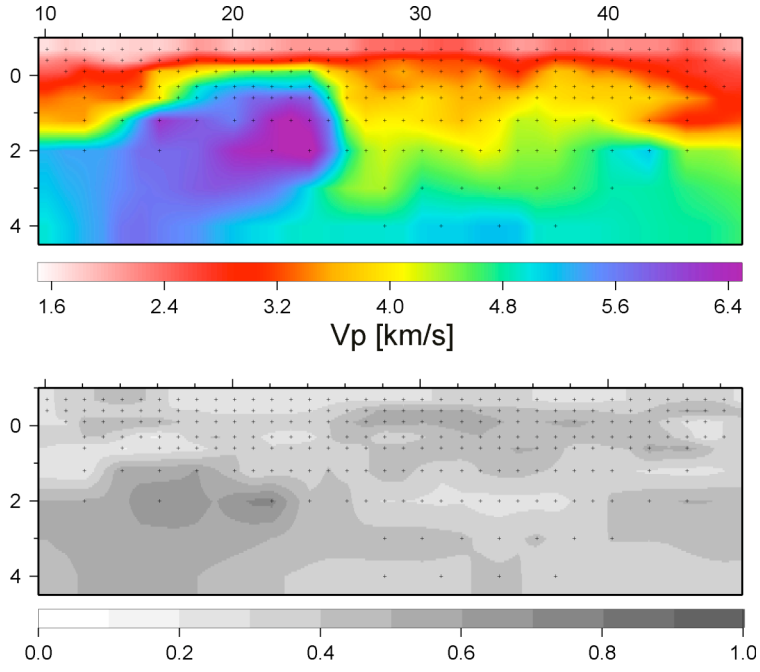

Figure 7: P-wave speed model from traveltime tomography (top) and corresponding diagonal elements of the resolution matrix. Small crosses are inversion nodes. The amplitude of the resolution values denotes the linear independence of a model parameter. Starting from a regular grid with variable axis spacing in z-direction, inversion nodes were iteratively removed from the grid, until all resolution values are greater than 0.2, a commonly accepted threshold (e.g. Kissling et al., 2001; Lippitsch et al., 2003). The grid note density of the final model gives an impression of the resolution. Penetration is deep on the right hand side of the model, and it is shallow on the left hand side, where the strong velocity contrast in the uppermost 1-2 km reflects much of the

energy. Below this contrast, the vertical velocity gradient is close to zero, if not negative, thus practically preventing deeper penetration.

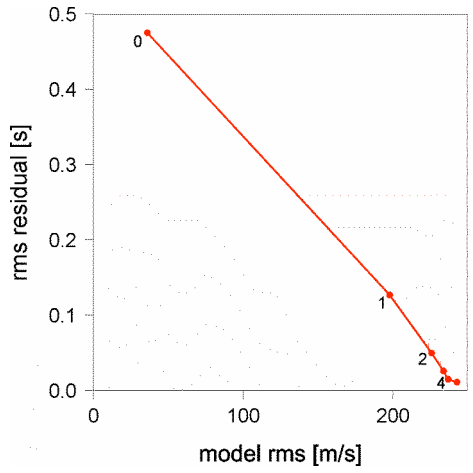

Figure 8: Traveltime residual versus lateral model heterogeneity. The starting model is 1D in the upper part, and it has a constant lateral gradient in the lower part. The curve is roughly linear in the first 4 iterations, and then flattens out indicating disproportionately large model changes for insignificant improvements. The inversion was stopped at the fifth iteration. The final traveltime residual is 0.01 s.

Waveform Inversion

Our waveform inversion strategy is almost identical to the one described by Bleibinhaus et al. (2007). We use a multi-scale approach to mitigate the non-linearities inherent to waveform inversion (Bunks et al., 1995; Pratt et al., 1996). We inverted 7 groups of increasingly higher frequency components of the data sequentially (Table 1) in order to reconstruct the model from coarse to fine wavelengths.

Frequencies [Hz]	Grid spacing [m]	Grid nodes	Wavelength filter [km]	Cost function reduction [%]
3.2, 3.6, 4.0	50	781x181	1.250	24.6 / 22.1
4.4, 4.8, 5.2	50	781x181	1.000	27.2 / 33.5
5.6, 6.0, 6.4	50	781x181	0.800	39.6 / 48.8
6.8, 7.2, 7.6	50	781x181	0.700	37.8 / 42.8
8.0, 8.8, 9.6	25	1525x361	0.500	40.8 / 37.2
10.4, 11.2, 12.0	25	1525x361	0.400	41.0 / 37.7
12.8, 13.6, 14.4	25	1525x361	0.250	32.6 / 35.4

Table 1: Waveform inversion parameters. The wavelength filter refers to the horizontal component of a 2D high-cut regularization filter with an aspect ratio of x:z = 4:1, which is applied to the gradient. The two values for the relative cost function reduction correspond to the inversion of flat-surface data and irregular-topography data respectively after 5 iterations. Note that the cost function measures the individual frequency group, not the overall misfit.

Each group was inverted for five iterations, and the resulting model was used as starting model for the inversion of the next group. The total computation time for the complete visco-acoustic frequency-domain waveform inversion amounts to one day on a single node, and it comprises more than 100 forward simulations. Note that for the visco-elastic time-domain code of Robertsson (1996) and irregular topography, the same inversion would require over three months on a 25-node cluster.

We used a common source signature for all shots, which we inverted simultaneously during the first iteration of each group. We performed tests varying the number of source inversion iterations, and the total number of iterations per group. Repeating the source inversion, or not, did not have much effect. A total of five iterations gave the best results in terms of recovering structure and avoiding artifacts. In another test we simultaneously inverted two frequencies out of the range 4-7 Hz along with each of the last three groups. This strategy is thought to stabilize the results, and it has been used by, e.g., Brenders and Pratt (2007). However, we found that the convergence was compromised, and the results were inferior.

Some of these differences may stem from a more fundamental difference. Instead of inverting true amplitude data, we inverted the phase of the complex frequency domain signal only. This essentially corresponds to trace normalization and spectral whitening. Note that the amplitude ratio of different arrivals within each trace is preserved in the phase of signal, assuming that the arrivals have a similar bandwidth. This amplitude normalization discards some of the geometrical spreading information of the data, but it also prevents those amplitude variations from degrading the results, that are not part of the forward model (e.g. when they are caused by intrinsic attenuation, or by topography), or that are simply too complex to be reconstructed during the first stages of waveform inversion. This approach was also taken for the inversion of the San-Andreas-Fault data (Bleibinhaus et al., 2007), and Shin and Min (2006) have demonstrated for the Rytov approximation that amplitudes are not crucial for waveform inversion.

We have done some preliminary tests using true amplitudes, and found that the reconstructions were not as good. However, more elaborate amplitude scaling may alter this result. We did not pursue this matter at this point, since we are mainly interested in comparing inversions of flat-surface and irregular-topography data.

For both inversions, subsurface parameters are simply extended in the air, and sources and receivers are embedded in the model at their true locations. In order to avoid wave propagation above ground, Q is gradually decreased from 1000 at 200 m below the receivers to 2 at 100 m above the receivers. Figure 9 displays the resulting waveform inversion models, along with the starting model and the true model.

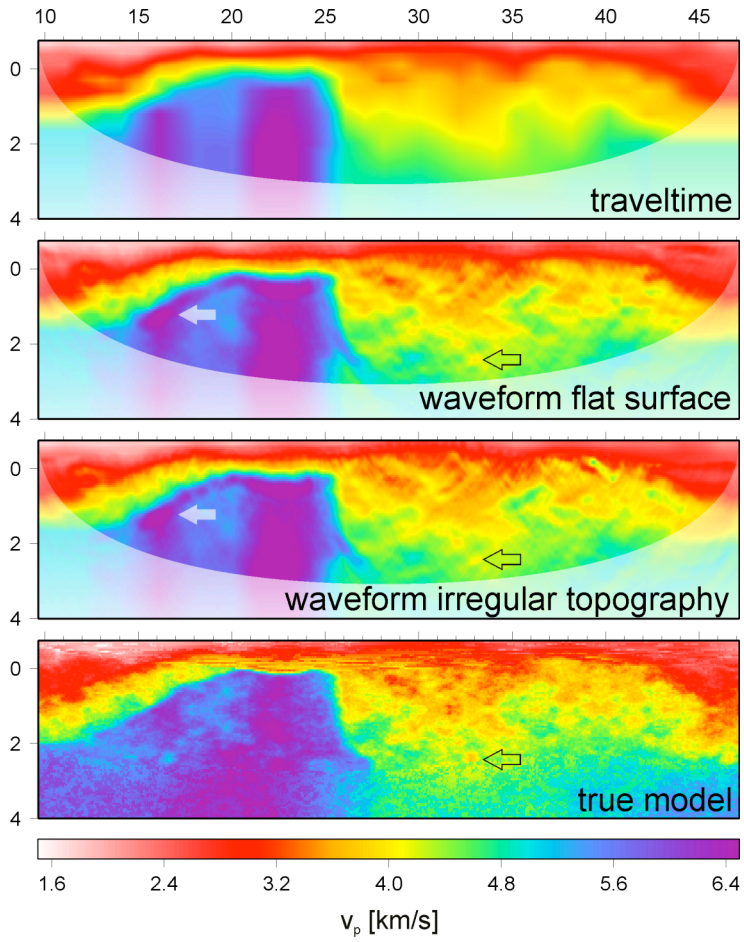

Figure 9: Starting model for waveform inversion derived by traveltime tomography, waveform inversion results for flat-surface data, for irregular topography data, and the true model (from top to bottom). White area is low subsurface coverage. Many structures, even at small scales are recovered from both datasets (hollow arrow). The top granite is better resolved than in the starting model, but the sharp contrast was not fully recovered, the velocities near the top of the granite are overestimated (white arrows), and its internal structure is not resolved. In addition, the waveform model from the irregular-topography data contains some shallow, localized, strong artifacts, particularly between km 39-45.

The inversion results derived from either dataset are relatively similar. They resolve detailed sediment structures (km 25-45), but hardly improve the image of the granite (km 10-25). Note that the resolution of the model from irregular-topography data is only slightly inferior. However, it exhibits some significant small scale artifacts near the surface. This assessment is confirmed by a more detailed comparison (Figure 10).

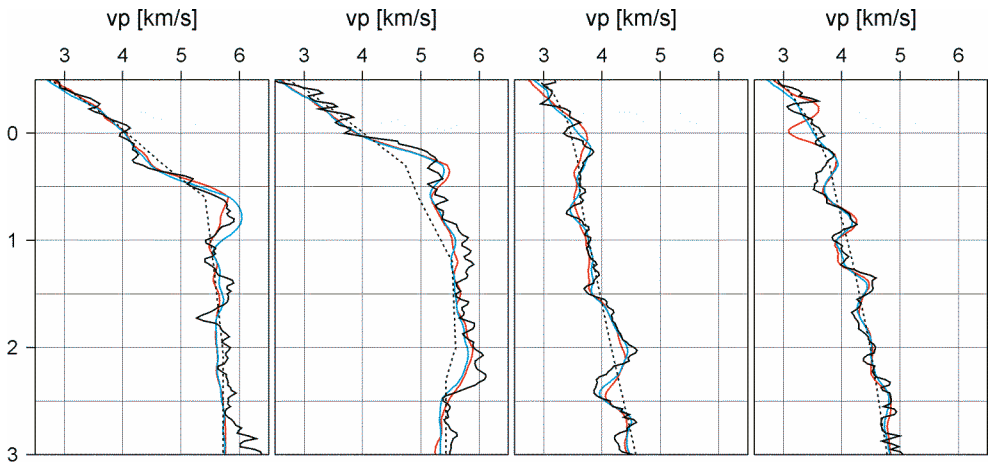

Figure 10: V(z) functions at ~ 7 km spacing (from left to right: km 18, 25, 33, 39). Dashed line is starting model, black line is true model low-pass filtered to the expected resolution, and blue and red lines are waveform models derived from flat-surface data and from irregular-topography data respectively. Apart from the shallow artifacts at km 39, the two models are quite similar and match the true model very well. However, the log at km 18 (in the granite) shows no resolution below 1 km depth. The log at the edge of the granite (km 25) shows that the starting model was improved at all depths, but the amplitude of the perturbations below 1 km depth is not matched. Even larger misfits in other parts of the granite are displayed in Figure 11.

The largest mismatch between the waveform models and the true model is observed at km 22, where the granite is very shallow. It is the result of reverberations, multiples and channeled waves in the sedimentary layer above the granite, which have not been modeled because the free surface was ignored. They appear as residuals in the objective function, and they are projected as artifacts onto the model. However, it was also impossible to exclude these phases from the inversion without excluding the bulk of the data, because at low frequencies those phases are barely separated from the first arrival. Of course, when the free-surface boundary condition is taken into account during the inversion, which can be done without additional computational expense for the flat-surface data, those mismatches are largely reduced (Figure 11). Remaining misfits at greater depth are probably the result of shallow penetration, and of very erroneous background velocities, and are not caused by errors in the forward modeling. Figure 12 shows the complete model derived by taking the free-surface boundary condition into account. It recovers some of the granites internal structure, and also exhibits the highest resolution in the sediments. Note that in order to match the relative amplitude of the various seismic phases generated by the strong velocity contrast and the free surface, the true Q model was supplied during the inversion. The importance of an accurate attenuation model in modeling multiples for waveform inversion was pointed out by Hicks and Pratt (2001).

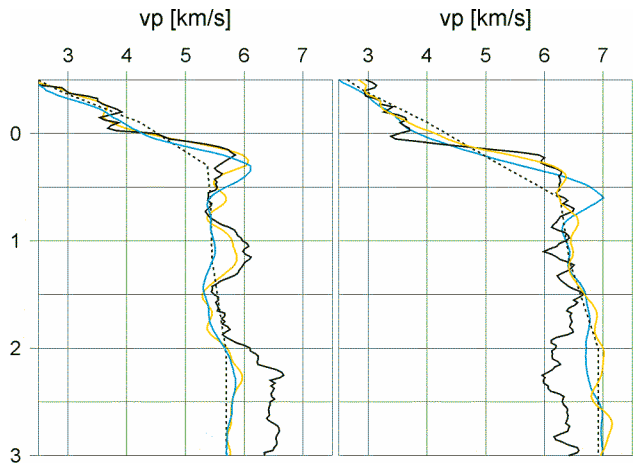

Figure 11: V(z) functions at km 20 (left) and km 22 (right). Dashed line is starting model, black line is true model filtered to the expected resolution, and blue and yellow lines are waveform models derived from flat-surface data using an absorbing-boundary condition, and a free-surface condition respectively. When the free surface is included, the top of the granite is matched very well, as is some of its internal structure. However, the misfit below 2 km depth remains large.

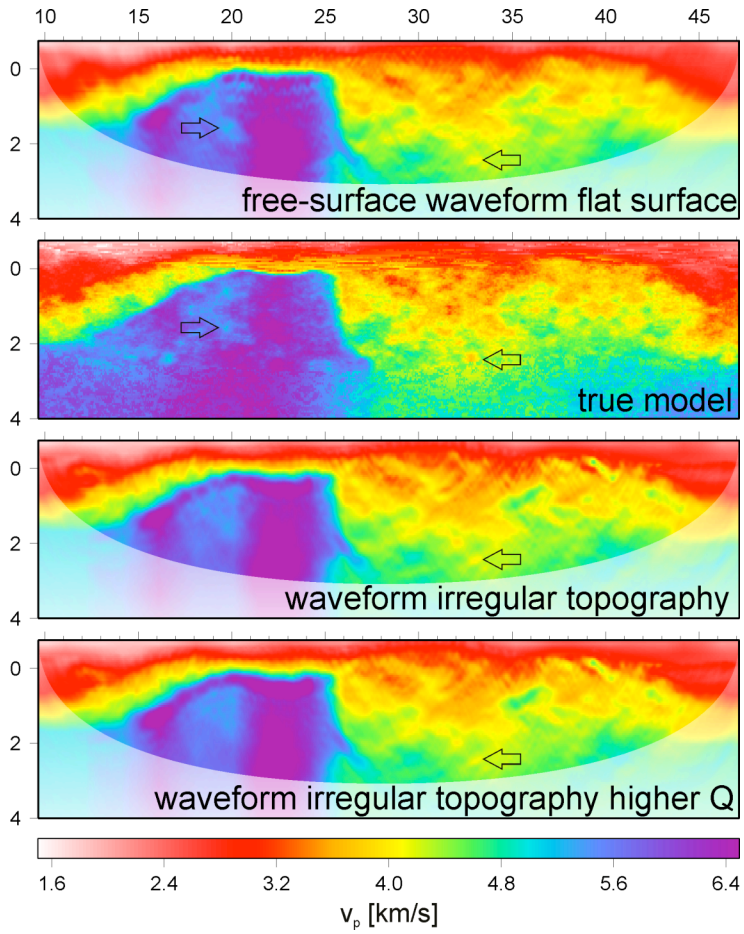

Figure 12: Waveform inversion of the flat-surface data taking the free-surface boundary condition into account, true model, and waveform inversions of irregular-topography data computed with the Q-model of Figure 3, and with higher Q-values (from top to bottom). The free-surface waveform model shows significantly less artifacts, a much better fit of the top granite, and it also reproduces some of the internal structure of the granite. The two irregular-

topography models are relatively similar. However, the resolution from higher-Q data is somewhat inferior.

Conclusions

The comparison of the waveform models from flat-topography data derived with and without taking the free-surface boundary condition into account (Figure 12, Figure 9) shows that the importance of this condition depends on the velocity structure. In the region of the model, where a thin low-velocity layer on top of a high velocity body produces strong reverberations, multiples, and channeled waves, ignoring the free-surface leads to a degraded recovery of the main velocity contrast, and to a total loss of resolution below. In the other region of the model, which shows no large first-order discontinuities, ignoring this condition leads to degraded resolution, but the resulting models are still dominated by real structures that could not be recovered by traveltime inversion. This is true irrespective of the topography. However, the scattering from irregular topography additionally introduces significant small scale artifacts near the surface when ignored in the inversion, and it also further decreases the resolution. It is nevertheless remarkable that ignoring free surface scattering does not necessarily lead to a breakdown of waveform inversion. In order to make sure that this conclusion is not biased by an extreme attenuation structure that unduly suppresses surface scattering, we computed and inverted another data set based on Q-values that are the double of those displayed in Figure 3. The comparison (Figure 12) exhibits a further slight decrease in resolution, but confirms that there is no breakdown.
The irregular topography used to synthesize some of the data was taken from a real survey, and the variations are strong and rough at all scales. However, it is not the most extreme topography, and we intend to synthesize and invert further surveys with even larger elevation variations. Further tests will also address the importance of a correct attenuation model, a point of crucial importance for the inversion of real data. Eventually, the goal will be to find a computationally inexpensive method to mimic irregular surface in order to increase the resolution of waveform inversion.

Acknowledgements

The authors want to thank Gerhard Pratt and Johann Robertsson for making their codes available to us. Support was provided by Shell Oil Company.

References

Bleibinhaus, F. and Gebrande, H., 2006. Crustal structure of the Eastern Alps along the TRANSALP profile from wide-angle seismic tomography. Tectonophysics, 414(1-4): 51-69.

Bleibinhaus, F., Hole, J.A., Ryberg, T. and Fuis, G., 2007. Structure of the California Coast Ranges and San Andreas Fault at SAFOD from seismic waveform inversion and reflection imaging. Journal of Geophysical Research, 112: B06315.

Brenders, A.J. and Pratt, R.G., 2007. Full waveform tomography for lithospheric imaging: results from a blind test in a realistic crustal model. Geophysical Journal International, 168(1): 133-151.

Bunks, C., Saleck, F.M., Zaleski, S. and Chavent, G., 1995. Multiscale Seismic Wave-Form Inversion. Geophysics, 60(5): 1457-1473.

Campman, X. and Riyanti, C.D., 2007. Non-linear inversion of scattered seismic surface waves. Geophysical Journal International, 171(3): 1118-1125.

Gao, F., Levander, A., Pratt, R.G., Zelt, C.A. and Fradelizio, G.L., 2007. Waveform tomography at a groundwater contamination site: Surface reflection data. Geophysics, 72(5): G45-G55.

Gardner, G.H.F., Gardner, L.W. and Gregory, A.R., 1974. Formation Velocity and Density - Diagnostic Basics for Stratigraphic Traps. Geophysics, 39(6): 770-780.

Gu, Y.J., Webb, S.C., Lerner-Lam, A. and Gaherty, J.B., 2005. Upper mantle structure beneath the eastern Pacific Ocean ridges. Journal of Geophysical Research-Solid Earth, 110(B6).

Hicks, G.J. and Pratt, R.G., 2001. Reflection waveform Inversion using local descent methods: Estimating attenuation and velocity over a gas-sand deposit. Geophysics, 66(2): 598-612.

Hole, J.A., 1992. Nonlinear High-Resolution 3-Dimensional Seismic Travel Time Tomography. Journal of Geophysical Research, 97(B5): 6553-6562.

Kaslilar, A., 2007. Inverse scattering of surface waves: imaging of near-surface heterogeneities. Geophysical Journal International, 171(1): 352-367.

Kissling, E., Husen, S. and Haslinger, F., 2001. Model parametrization in seismic tomography: a choice of consequence for the solution quality. Physics of the Earth and Planetary Interiors, 123(2-4): 89-101.

Lippitsch, R., Kissling, E. and Ansorge, J., 2003. Upper mantle structure beneath the Alpine orogen from high-resolution teleseismic tomography. Journal of Geophysical Research-Solid Earth, 108(B8).

Operto, S. et al., 2004. Quantitative imaging of complex structures from dense wide-aperture seismic data by multiscale traveltime and waveform inversions: a case study. Geophysical Prospecting, 52(6): 625-651.

Operto, S., Virieux, J., Dessa, J.X. and Pascal, G., 2006. Crustal seismic imaging from multifold ocean bottom seismometer data by frequency domain full waveform tomography: Application to the eastern Nankai trough. Journal of Geophysical Research-Solid Earth, 111(B9).

Pratt, R.G., 1999. Seismic waveform inversion in the frequency domain, Part 1: Theory and verification in a physical scale model. Geophysics, 64(3): 888-901.

Pratt, R.G., Song, Z.M., Williamson, P. and Warner, M., 1996. Two-dimensional velocity models from wide-angle seismic data by wavefield inversion. Geophysical Journal International, 124(2): 323-340.

Ravaut, C. et al., 2004. Multiscale imaging of complex structures from multifold wide-aperture seismic data by frequency-domain full-waveform tomography: application to a thrust belt. Geophysical Journal International, 159(3): 1032-1056.

Robertsson, J.O.A., 1996. A numerical free-surface condition for elastic/viscoelastic finite-difference modeling in the presence of topography. Geophysics, 61(6): 1921-1934.

Robertsson, J.O.A., Blanch, J.O. and Symes, W.W., 1994. Viscoelastic Finite-Difference Modeling. Geophysics, 59(9): 1444-1456.
Robertsson, J.O.A. and Holliger, K., 1997. Modeling of seismic wave propagation near the earth's surface. Physics of the Earth and Planetary Interiors, 104(1-3): 193-211.
Shin, C. and Min, D.J., 2006. Waveform inversion using a logarithmic wavefield. Geophysics, 71(3): R31-R42.
Sirgue, L. and Pratt, R.G., 2004. Efficient waveform inversion and imaging: A strategy for selecting temporal frequencies. Geophysics, 69(1): 231-248.
Xu, Y.B. and Wiens, D.A., 1997. Upper mantle structure of the southwest Pacific from regional waveform inversion. Journal of Geophysical Research-Solid Earth, 102(B12): 27439-27451.